Additive Manufacturing Letters 18 (2026) 100381

Contents lists available at ScienceDirect

Additive Manufacturing Letters

journal homepage: www.elsevier.com/locate/addlet

Short Communication

Effect of thermal treatments on a MAPS-printed Cr–Mo–Ni alloy steel

S. Marola [a,*], W. Zhang [b,c,*], R. Lupoi [b], R. Casati [a]

[a] Politecnico di Milano, Department of Mechanical Engineering, Via la G. La Masa 1, 20156 Milano, Italy
[b] Trinity College Dublin, The University of Dublin, Department of Mechanical, Manufacturing & Biomedical Engineering, Dublin, Ireland
[c] State Key Laboratory for Manufacturing Systems Engineering, Xi'an Jiaotong University, Xi'an, Shaanxi, 710049, China

ARTICLE INFO

Keywords:
Metal additive manufacturing using powder sheet (MAPS)
Thermal treatment
Microstructure
Mechanical Properties

ABSTRACT

This study explores the influence of post-processing heat treatments on the microstructure and mechanical properties of a Cr–Mo–Ni alloy steel fabricated via Metal Additive Manufacturing using Powder Sheet (MAPS). Thermo-Calc simulations and differential scanning calorimetry analysis were performed to define solution and tempering conditions. The as-built samples exhibited near-full density and increased carbon content compared to that of feedstock material due to binder decomposition and C pick-up during printing. Austenitizing at 1000 °C followed by water quenching produced a martensitic microstructure with uniform elemental distribution. Subsequent tempering between 200 °C and 600 °C induced carbide precipitation within martensitic laths. X-ray diffraction and electron microscopy analysis confirmed complete carbide dissolution after austenitizing and their re-precipitation during tempering, with finer carbides than those found in the as-built state. Austenitizing and water quenching led to an increase in hardness of 300 HV, while tempering induced a gradual decrease, remaining above the as-built levels up to 400 °C. These results demonstrate that tailored thermal treatments can effectively enhance the mechanical performance of MAPS-printed steels by controlling microstructural evolution.

1. Introduction

Over the past decade, additive manufacturing (AM) technologies have gained increasing attention for the production of metallic components due to their ability to create complex geometries, reduce production times, and enable material customization. These processes allow precise control over the microstructure of metals, directly influencing key mechanical properties such as hardness, strength, and toughness. However, as-built (AB) materials often exhibit inherent defects, such as residual porosity, chemical segregation, or non-optimal microstructures, which can limit their performance compared to conventionally manufactured materials [1,2]. Understanding the relationships between process parameters, microstructure, and mechanical properties is therefore essential for developing effective post-processing strategies and achieving high-performance metallic components [3,4].

Among the main AM routes for metallic alloys, laser powder bed fusion (PBF-LB/M) and directed energy deposition (DED) have been extensively studied, highlighting both their potential and their intrinsic limitations, including anisotropy, porosity, and residual stresses. In this context, Metal Additive Manufacturing using Powder Sheet (MAPS) has recently emerged as an innovative approach that employs powder sheets composed of metal particles embedded within a polymeric binder, integrating concepts from both PBF-LB/M and sheet lamination [5,6]. The elimination of loose powder provides MAPS with several advantages over conventional PBF processes: (i) reduced material consumption and minimal waste thanks to easy recycling of powder sheets; (ii) improved safety during storage and transportation, eliminating health hazards related to the use of micrometric powders; (iii) prevention of cross-contamination between different materials due to the absence of loose powder; (iv) the ability to fabricate multi-material components in a single step and within a single AM system. Moreover, since MAPS does not rely on powder flow for layer deposition, it allows the use of powders that are challenging for PBF-LB/M, such as those produced via water atomization, which are typically less spherical and have lower flowability [7–9].

Recent studies by Zhang et al. [10] and Sasnauskas et al. [11] have reported carbon uptake during the MAPS printing process, which may influence the chemical composition, microstructure, and thermal response of the final material. In MAPS-printed 304 stainless steel, Zhang et al. observed an increase in carbon content of 1.10 wt %, resulting in the formation of a coarser carbide network and enhanced mechanical strength compared to PBF-LB/M-printed 304SS. This

* Corresponding authors.
E-mail addresses: silvia.marola@polimi.it (S. Marola), wenyouzhang@mail.xjtu.edu.cn (W. Zhang).

https://doi.org/10.1016/j.addlet.2026.100381
Received 23 January 2026; Received in revised form 8 April 2026; Accepted 30 April 2026
Available online 1 May 2026

behavior has been associated with in-process alloying mechanisms, in which the polymeric binder decomposes under laser irradiation and releases carbon species that diffuse into the molten pool.

Sasnauskas et al. observed similar behavior in CoNiCrFeMn high-entropy alloys (HEAs), systematically investigating polymer contents from 5 wt % to 30 wt % in the powder sheet. Their results demonstrated that increasing polymer content raises the retained carbon in the printed alloy. The study also showed that sheet orientation affects carbon pickup, with higher retention when the polymer side faces away from the laser due to longer interaction with the molten pool. These findings confirm that binder-derived carbon incorporation is a fundamental characteristic of MAPS, with implications for achievable microstructures and post-processing behavior.

As a consequence, both the microstructure and the response to post-processing heat treatments may differ from those of the nominal alloy, requiring careful evaluation of the material state prior to heat treatment. Nevertheless, the available literature on the effects of heat treatments on MAPS-fabricated alloys remains limited. This aspect is particularly relevant, as effective post-processing is essential for optimizing microstructure and mechanical properties, while conventional heat treatments developed for the original alloy cannot be directly transferred due to the modified composition and solidification conditions. In the context of MAPS processing, the selection of the metallic feedstock becomes a strategic design lever. Alloy compositions can be tailored to account for process-induced carbon incorporation, thereby exploiting its strengthening potential while avoiding the formation of undesirable phases or excessive brittleness.

In this study, a water atomized Fe-Cr-Mo-Mn-Ni low-alloy steel powder with very low carbon content (C = 0.005 wt%) was selected as the powder sheet feedstock. Its processability using conventional PBF-LB/M techniques has been demonstrated by Abdelwahed et al. in [12]. After MAPS processing, the expected carbon pickup allows the material to reach a final composition approaching that of a bearing steel, enabling tailored microstructure and mechanical properties through post-processing.

Building on this material design strategy, this study focuses on evaluating the response of MAPS-processed steel to heat treatment. To this end, a combined computational and experimental approach was adopted. Thermodynamic simulations using Thermo-Calc and differential scanning calorimetry (DSC) tests on the AB samples were first performed to identify suitable heat-treatment schedules. Drawing on traditional steel practices, austenitizing, quenching, and tempering at various temperatures were applied. Subsequent microstructural characterization by electron microscopy and X-ray diffraction (XRD) and hardness testing were performed to evaluate the effect of the heat treatments. The ultimate goal is to optimize the thermal cycle specifically for this MAPS-fabricated material, ensuring that the final microstructure and mechanical properties fully exploit the benefits of carbon uptake and alloy design. The expected outcome is to establish guidelines for developing post-processing routes for MAPS components, enabling heat-treatment strategies that maximize performance and reliability.

2. Materials and methods

2.1. Powder and powder sheet preparation

The steel powder used for the production of the powder sheets, with the nominal composition reported in Table 1, was supplied by Höganäs AB. The powder, characterized by a particle size distribution of 20–63 μm, was produced via water atomization and subsequently subjected to a controlled oxygen-reduction process to improve chemical purity.

Table 1
Nominal chemical composition of the steel powder provided by Höganäs AB in wt%.

C	Cr	Mo	Si	Mn	Ni	O	Fe
0.005	3.10	0.51	0.03	0.06	0.48	0.159	Bal.

Powder sheets for the MAPS process were prepared via a solvent casting technique [13,14]. Polycaprolactone (PCL, $(C_6H_{10}O_2)_n$) pellets were dissolved in chloroform ($CHCl_3$) to form a polymer solution, which was subsequently mixed with the steel powder to obtain a homogeneous metal-polymer-solvent dispersion. The dispersion was cast onto a moving flat surface using a 90° beveled razor blade to precisely control the sheet thickness. Upon solvent evaporation, a flexible and cohesive film, hereafter referred to as the powder sheet, was obtained.

As shown in Fig. 1a–b, the PCL binder effectively encapsulated the irregularly shaped metallic particles, maintaining their cohesion and preventing powder loss at room temperature, thus providing a stable and safe feedstock for MAPS processing.

2.2. MAPS processing

The MAPS printing process, schematically illustrated in Fig. 1c, was carried out using a Realizer SLM50 system equipped with a continuous-wave fiber laser operating at a 1064 nm wavelength. The optimised process parameters employed for MAPS printing included a laser power of 100 W, a scan speed of 200 mm/s, a laser spot size of 140 μm, and a hatching spacing of 100 μm. For the first layer, the powder sheet was placed directly onto a 304SS base plate, and the laser scanned the predefined area. After each layer, the build plate was lowered by 20 μm, a value selected accounting for the shrinkage occurring during the melting-solidification sequence.

Between subsequent layers, the inert gas (argon) flow was temporarily interrupted to allow manual placement of a new powder sheet via glove box. The printing cycle resumed once the concentration of oxygen inside the chamber dropped below 0.24%. This procedure was repeated to fabricate 22 samples with nominal dimensions of 5 × 5 × 1 mm^3 (Fig. 1d).

Following the printing, the MAPS-printed samples were detached from the building platform using electrical discharge machining (EDM). The carbon content in the as-built alloy was determined by Inductively Coupled Plasma – Optical Emission Spectroscopy (ICP–OES) prior to defining any heat treatment.

2.3. Sample characterization and heat treatment

Sample porosity was evaluated by optical microscopy (Nikon Eclipse LV150NL equipped with a DS-U3 camera, NIS Elements v4.60). For each sample, thirty micrographs were acquired at 50X magnification, converted to grayscale, and binarized using ImageJ. Manual correction was applied to remove artifacts and ensure accurate segmentation of pores. The resulting binary images were then analyzed to determine the porosity fraction, calculated as the ratio of pore area to total analyzed area.

A combined computational and experimental approach was employed to support the design of post-processing heat treatments for the MAPS-processed steel. Thermodynamic calculations were carried out using Thermo-Calc 2023b, coupled with the TCFE12 (Steels/Fe-Alloys v.12.0) database and the MOBFE8 mobility database. DSC analyses were conducted using a Setaram Themys One instrument under a 20 ml min^{-1} argon flux in a temperature range spanning from 200 °C to 1200 °C at a heating rate of 10 °C min^{-1}. The heat flux was equilibrated both at low and high temperature.

Based on the thermodynamic simulation results and DSC analyses, a series of heat treatment routes were designed to investigate the thermal response of the MAPS-processed steel. The thermal treatments were carried out using a Lenton UAF 27/14 furnace (maximum temperature 1400 °C) and a Carbolite HRF furnace (maximum temperature 750 °C). All the selected heat treatments were conducted in air, while quenching, when required, was performed in still water at room temperature.

Microstructural analyses were performed using a Zeiss Sigma 500

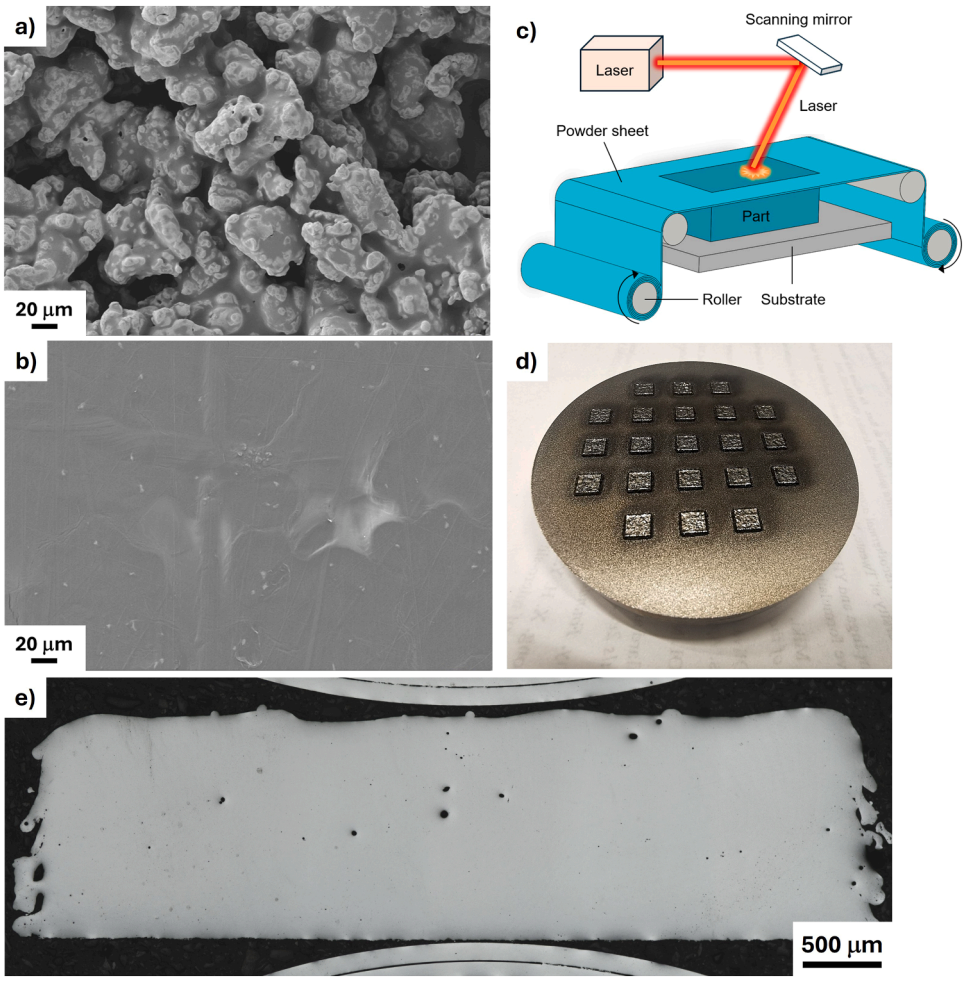

Fig. 1. Powder sheet morphology respectively on powder side(a) and binder side (b). Scheme of the MAPS process (c) and picture of the steel samples printed by MAPS onto the build platform (d) and in cross section (e).

Field Emission Scanning Electron Microscope (FE-SEM) equipped with an Oxford Instruments Ultim Max energy dispersive X-ray spectroscopy (EDS) detector. Samples for microstructural investigations were hot-mounted in a conductive resin (EP16 Hitech Europe), then ground using SiC papers of progressively finer grit and polished using diamond suspensions (6 µm, 3 µm, and 1 µm). Final polishing was done using a colloidal silica suspension to achieve a mirror-like finish.

To reveal the microstructure, the specimens were etched by immersion using a 1:1:1 solution of distilled water: HNO_3: HCl for 6 s. Phase identification was carried out by X-ray diffraction (XRD) using a Rigaku SmartLab SE multipurpose diffractometer equipped with a Cu K_α radiation source. Measurements were performed in Bragg-Brentano geometry over the 2θ range from 20° to 100° at a scanning rate of 1.5° min^{-1} and using a 0.02° step size.

Vickers microhardness measurements were performed on polished samples using a Future Tech FM-810 microhardness tester. A load of 1000 gf (HV_1) and a dwell time of 15 s were applied. The reported hardness numbers correspond to the mean of at least five independent indentations per condition.

3. Results and discussion

3.1. Evaluation of MAPS-printed samples

As shown in Fig. 1d, the MAPS process successfully produced the steel samples. A microstructural evaluation of the MAPS samples revealed high densification levels (99.4%), with residual porosity primarily attributed to trapped gas rather than lack-of-fusion defects (Fig. 1e), indicating satisfactory melting and consolidation under the selected laser processing conditions.

Since carbon pickup due to the decomposition of the polymeric binder during laser melting has been reported as an intrinsic feature of the MAPS process, including in alloy systems different from the one investigated here [10,11], the actual carbon content of the MAPS-printed samples was quantified directly after printing using the ICP-OES analysis. The carbon content was measured on multiple MAPS-printed samples (approximately ten), yielding to an average concentration of about 0.95 wt%.

The final alloy composition of the MAPS-printed steel here investigated approaches that of a bearing steel, suggesting that MAPS processing can transform initially low-carbon feedstock into materials with enhanced hardness and wear resistance.

This compositional transformation opens up new opportunities for tailoring performance through process-induced alloying, enabling the production of components with improved properties. MAPS-fabricated steels enriched in carbon could therefore find application in tooling, tribological components, or functionally graded structures, where controlled variations in local composition and properties are advantageous. At the same time, such in-process alloying necessitates a careful reassessment of post-processing strategies, since both the microstructure and the mechanical behavior now depend on the newly developed chemistry rather than on that of the original feedstock.

3.2. Heat treatment design

Given the modified chemical composition resulting from the carbon enrichment during printing, the definition of appropriate heat treatment parameters for the MAPS-processed steel required the combination of computational and experimental approaches.

To this end, Thermo-Calc simulations, using the experimentally determined composition of the MAPS-printed samples as input, were first employed to predict the equilibrium phase evolution with temperature, providing an initial guideline for selecting the most suitable heat treatment conditions. The calculated phase stability diagram (Fig. 2a) revealed that temperatures around 1000 °C enable the complete dissolution of the carbides ($M_{23}C_6$, M_7C_3) likely formed during the MAPS process, while preserving a fully austenitic structure (Fe-FCC). This temperature was therefore selected as the austenitizing temperature, with the dual objective of fully transforming the microstructure into austenite prior to quenching and promoting microstructural homogenization by reducing segregation and eliminating secondary phases induced by the printing process.

Considering that the typical thermal treatments for C-bearing steels involve quenching from temperature higher than A3 and tempering (usually in the temperature range of 200 °C to 600 °C), two main types of thermal cycles were designed for experimental validation: (i) a austenitizing at 1000 °C for 15 min followed by water quenching to promote the formation of a hard martensitic microstructure; and (ii) a austenitizing followed by water quenching and subsequent tempering at various temperatures (200 °C, 300 °C, 400 °C, 500 °C, and 600 °C) for 30 min to systematically investigate the microstructural and mechanical evolution upon tempering. The short soaking times were chosen considering the small sample dimensions, to minimize excessive grain

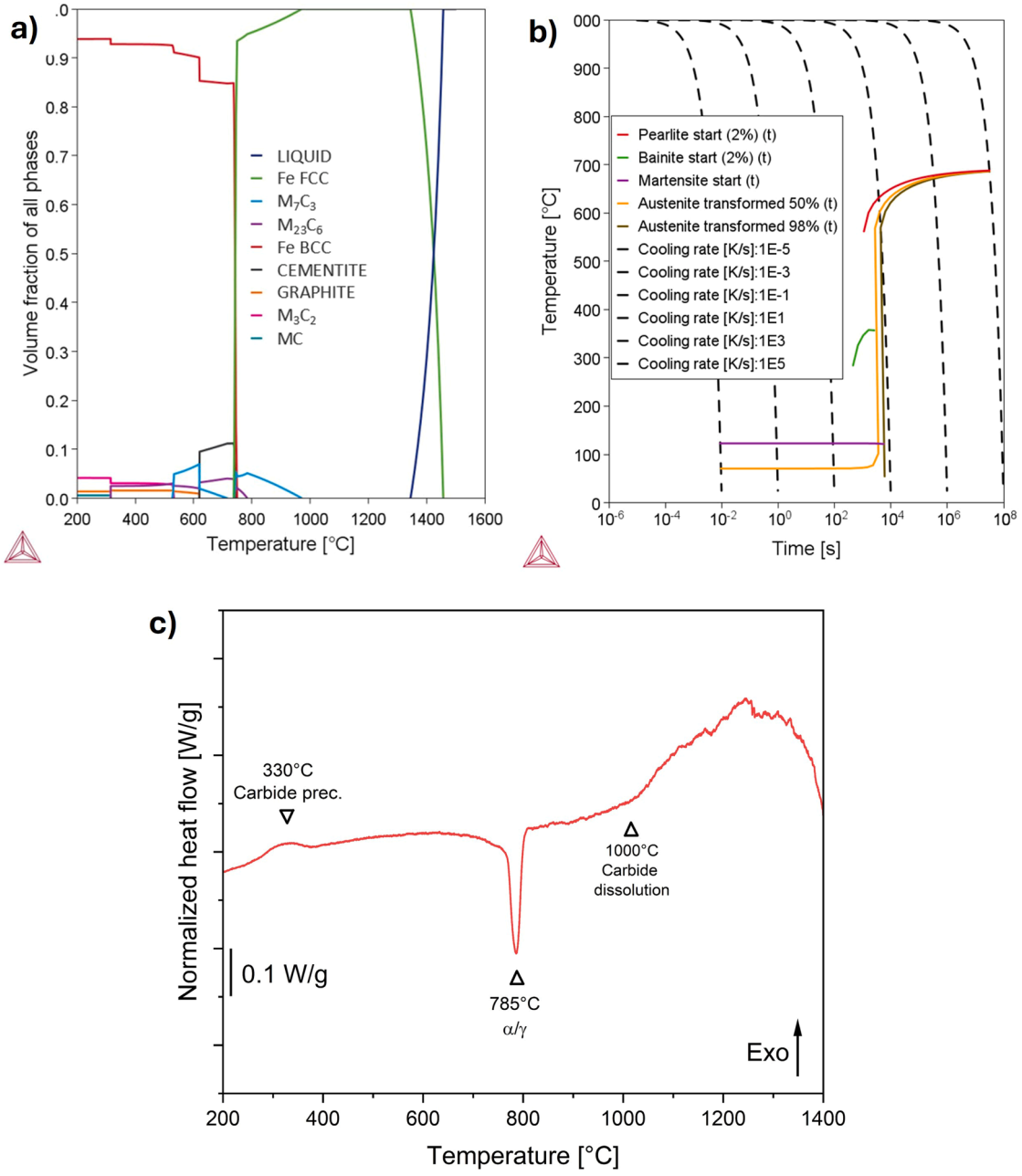

Fig. 2. Equilibrium phase evolution of MAPS-printed samples (a) and simulated CCT curves for the same steel (b). DSC curve of the MAPS-printed steel in the temperature range of interest for the selection of the thermal treatment (c).

growth while ensuring full phase transformation.

To gain further insight into the expected microstructural development occurring during quenching, the Continuous Cooling Transformation (CCT) curves of the MAPS-processed steel were simulated using Thermo-Calc (Fig. 2b), assuming a austenitizing temperature of 1000 °C and an austenitic grain size of 10 μm. The austenitic grain size adopted for the simulations was selected based on previous experimental and modelling studies performed on comparable steel systems processed under similar conditions. The resulting curves indicated that martensite is the predominant phase upon cooling at rates higher than 10 °C s^{-1}, consistent with the carbon-enriched composition.

Before performing the actual heat treatments, a DSC analysis was carried out on the as-built MAPS sample to experimentally verify the thermal events predicted by the thermodynamic model and to confirm the suitability of the selected austenitizing temperature. The DSC curve (Fig. 2c) exhibited an exothermic peak at 330 °C, corresponding to carbide-related tempering reactions, possibly including M_3C precipitation and/or retained austenite decomposition [15], followed by a distinct endothermic peak at 785 °C, associated with the phase transformation from Fe-α to Fe-γ [12]. Above this temperature, a broad endothermic region was observed, with a maximum centered around 1000 °C, indicating the dissolution of carbides formed during the in-process alloying and intrinsic heat treatment typical of laser-based AM processes [16]. Overall, the DSC results are in good agreement with the Thermo-Calc equilibrium simulations, although some discrepancies in the exact transformation temperatures are evident, particularly with respect to carbide dissolution. These differences are expected, as the experimental DSC measurements reflect dynamic, non-equilibrium conditions, whereas the simulations assume thermodynamic equilibrium. Nevertheless, the combined experimental and computational results confirm that 1000 °C is an appropriate temperature to ensure extensive carbide dissolution and the attainment of a fully austenitic microstructure prior to quenching.

On this basis, the proposed thermal cycles, namely austenitizing followed by quenching and austenitizing followed by quenching and tempering at different temperatures, were confirmed and subsequently applied to the MAPS-fabricated samples. The MAPS-processed samples subjected to these selected heat treatments were subsequently analyzed to determine how each condition affects the microstructure and mechanical behavior, with the goal of identifying the optimal post-processing route.

3.3. *Microstructural and phase evolution of the MAPS-printed samples upon heat treatment*

Fig. 3 presents the microstructures of the MAPS-processed steel samples in the as-built condition and following the various heat treatments. A marked difference is evident between the AB and heat-treated conditions. In the AB sample, the microstructure is characterized by Fe-rich cells surrounded by a thick network of carbides enriched in Cr and Mo, as confirmed by the EDS maps in Fig. 4. This carbide network reflects the combined effect of the carbon uptake during printing and the segregation phenomena occurring during rapid solidification, highlighting the influence of in-process alloying on the initial microstructural state.

Following the austenitizing at 1000 °C and water quenching, the microstructure transforms into a predominantly martensitic matrix, with no carbides detected in either the secondary electron images or the corresponding EDS maps (Figs. 3 and 4). This confirms that the selected treatment conditions effectively dissolve the carbides formed during printing, homogenizing the alloy and preparing it for controlled tempering.

When tempering treatments are applied, carbide precipitation is clearly observed in the micrographs (Fig. 3). The size and distribution of these carbides are strongly dependent on the tempering temperature: higher temperatures promote coarser precipitates, reflecting classical tempering behavior in C-rich steels. Due to their submicrometric and nanometric dimensions, precise compositional identification of these carbides by SEM-EDS was not feasible; however, the elemental maps indicate a relatively homogeneous distribution of Cr, Mo, and Fe in the matrix surrounding the precipitates, suggesting that the carbides are well-dispersed and consistent with expectations for tempering-induced precipitation.

To further investigate the phase constitution of the MAPS-printed steel, XRD analyses were conducted on the AB and heat-treated samples. The diffraction patterns (Fig. 5) show that, in the AB sample, the reflections are consistent with a ferritic/martensitic phase and carbides, along with small amounts of retained austenite, consistent with the microstructural observations of Fe cells surrounded by a carbide network. After quenching, the diffraction peaks corresponding to austenite and carbides completely disappear, leaving only the reflections of the martensitic phase, which confirms the complete dissolution of carbides during the solubilization treatment. In tempered steel samples, carbide reflections reappear in the XRD patterns alongside reflections from the ferritic/martensitic phases indicating carbide precipitation. These results demonstrate that the carbides forming during tempering are of the same type as those initially present in the AB condition. Precise identification of the individual carbide phases though remains challenging, as the observed peaks are compatible with the carbide phases predicted by Thermo-Calc, but none exhibits a sufficiently distinctive fingerprint to allow an unambiguous phase assignment, likely due to the nanometric size of the precipitates and

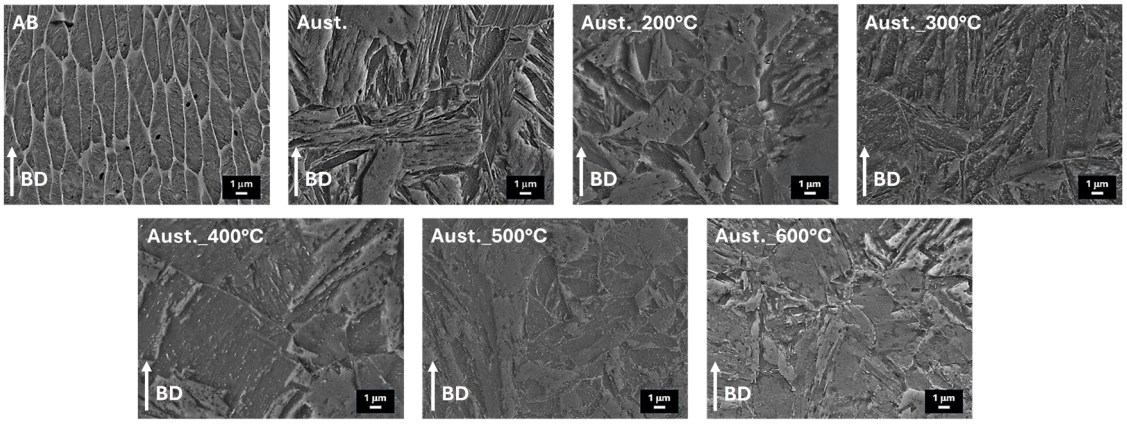

Fig. 3. Microstructures of the low carbon steel samples in both AB condition and after heat treatment. In particular AB refers to the microstructure originating after MAPS-printing, Aust. to the sample kept at 1000 °C for 15 min followed by water quenching, while Aust._xxx °C refer to the sample subjected first to the Aust. thermal treatment and later tempered for 30 min at different temperatures from 200 to 600 °C.

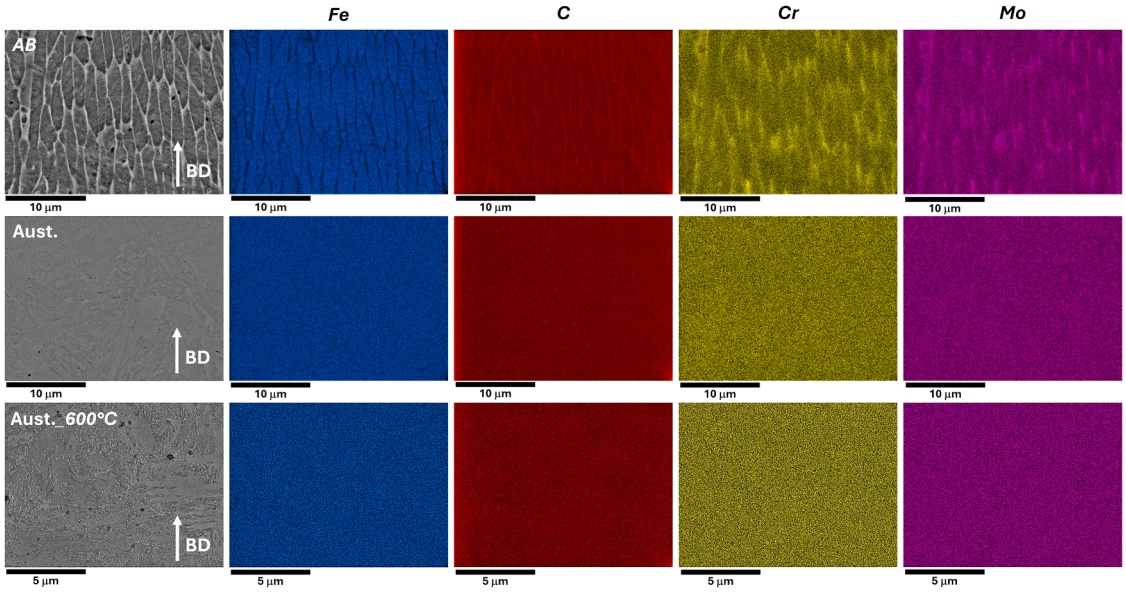

Fig. 4. EDS maps of the low carbon steel samples in both as-built condition and after heat treatment. In particular AB refers to the microstructure originating after MAPS-printing, Aust. to the sample kept at 1000 °C for 15 min followed by water quenching, while Aust._600 °C refer to the sample subjected first to the Aust. thermal treatment and later tempered for 30 min at 600 °C.

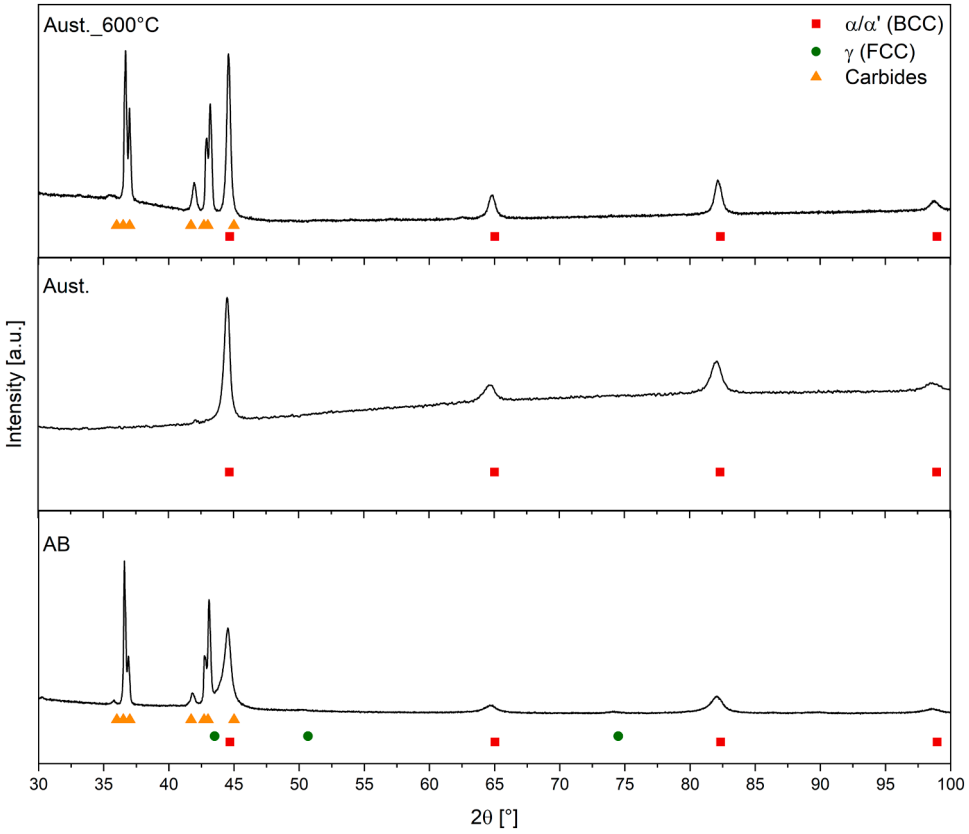

Fig. 5. XRD patterns of the low carbon steel samples in both as-built condition and after heat treatment. In particular AB refers to the microstructure originating after MAPS-printing, Aust. to the sample kept at 1000 °C for 15 min followed by water quenching, while Aust._600 °C refer to the sample subjected first to the SHT thermal treatment and later tempered for 30 min at 600 °C.

limitations in the phase database used.

Overall, the phase transformation sequences predicted by the Thermo-Calc simulations (Fig. 2a and b) are in good agreement with the experimentally obtained results, supporting the reliability of the computational approach for capturing the main transformation pathways in MAPS-processed steels. However, although the experimental results confirm the occurrence of carbide formation, they do not allow an unambiguous identification of the specific carbide types formed.

These results collectively demonstrate that the carbon uptake during printing strongly influences both the as-built microstructure and the subsequent response to heat treatment, reinforcing the importance of tailored post-processing strategies to achieve the desired combination of strength, hardness, and microstructural stability.

3.4. Mechanical response of the heat treated MAPS-printed specimens

Vickers microhardness measurements were employed to evaluate the evolution of the mechanical response of the steel under the different heat treatment routes. The results, reported in Fig. 6, indicate that the applied heat treatments significantly influence the hardness of the material. Notably, the relatively high hardness of the AB condition is consistent with the marked carbon enrichment induced by the MAPS process, as the starting low-carbon material exhibited a hardness of only 184 ± 5 HV [12]. In particular, austenitizing followed by quenching leads to the highest hardness number, consistent with the formation of a predominantly high-C martensitic microstructure. Subsequent tempering treatments progressively reduce hardness as the temperature rises, reflecting the expected softening associated with carbide coarsening and tempering of the martensitic matrix [17]. Despite this reduction, hardness values remain higher than those of the AB sample up to a tempering temperature of 400 °C, demonstrating that tempering can be used to tune hardness without completely compromising the strength.

According to established correlations between hardness and mechanical properties in steels (ultimate tensile strength UTS [MPa] ≈ 3.45·HV), the observed trends suggest that higher hardness achieved after quenching corresponds to UTS and reduced ductility, whereas tempering provides a controlled reduction in hardness accompanied by a likely increase in plasticity. These findings underscore the effectiveness of tailored heat treatment in optimizing the trade-off between strength and toughness in MAPS-fabricated steels, taking into account the carbon enrichment introduced during the printing process.

These observations validate the proposed methodology as a robust tool for selecting and optimizing post-processing parameters for MAPS-fabricated steels, demonstrating that careful integration of simulation and experimental analysis can effectively tailor microstructure and mechanical performance even in alloys modified by in-process carbon uptake.

4. Conclusions

This study examined the effect of post-processing thermal treatments on a MAPS-printed Cr–Mo–Ni alloy steel. Despite occasional process instabilities, MAPS enabled the fabrication of highly dense samples (≈ 99.4%), while binder decomposition led to significant carbon enrichment (from 0.005 wt% to 0.95 wt%), effectively shifting the alloy composition toward that of a bearing steel.

On the basis of the experimentally determined composition, a combined thermodynamic and experimental approach was used to design appropriate heat treatments to follow the MAPS printing process. Thermo-Calc simulations and DSC analyses identified 1000 °C as a suitable austenitizing temperature to ensure extensive carbide dissolution and full austenitization prior to quenching. Quenching resulted in a predominantly high-carbon martensitic microstructure, whereas subsequent tempering between 200 and 600 °C promoted controlled carbide precipitation.

Microstructural, phase, and hardness analyses showed good agreement with the simulated transformation pathways. Quenching maximized hardness, while tempering enabled effective tuning of the mechanical response, maintaining hardness values higher than the as-built condition up to 400 °C. Overall, the results demonstrate that accounting for process-induced compositional changes is essential for the rational design of heat treatments in MAPS-fabricated steels and confirm the potential of MAPS for producing high-performance Cr–Mo–Ni steels through tailored thermal processing.

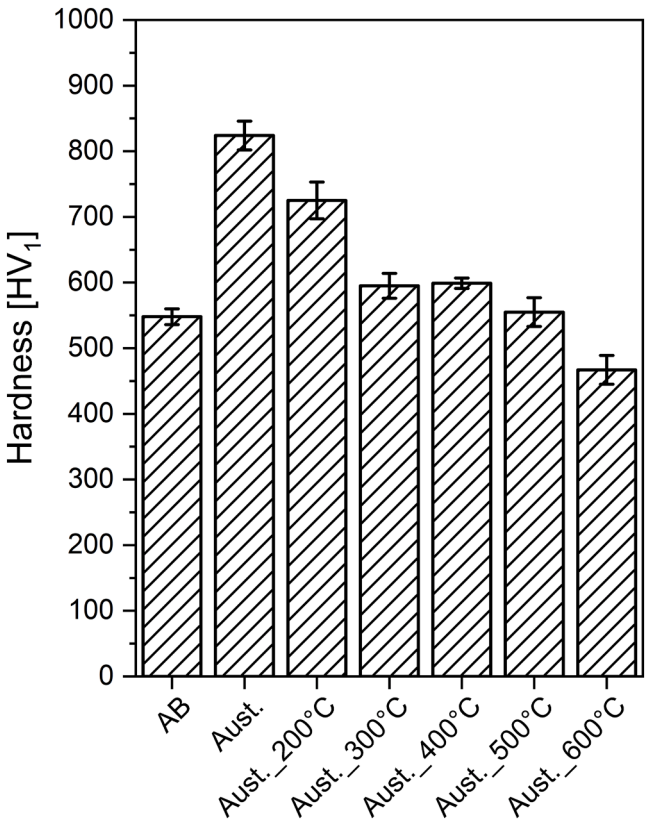

Fig. 6. Vickers microhardness of the MAPS-printed LCS both in the as-built condition and after the attempted thermal treatments. In particular AB refers to the microstructure originating after MAPS-printing, SHT to the sample kept at 1000 °C for 15 min followed by water quenching, while SHT_xxx °C refer to the sample subjected first to the SHT thermal treatment and later tempered for 30 min at different temperatures from 200 to 600 °C.

CRediT authorship contribution statement

S. Marola: Writing – original draft, Methodology, Investigation, Conceptualization. **W. Zhang:** Writing – review & editing, Investigation. **R. Lupoi:** Writing – review & editing, Project administration. **R. Casati:** Writing – review & editing, Funding acquisition.

Declaration of competing interest

The authors declare the following financial interests/personal relationships which may be considered as potential competing interests:

Rocco Lupoi, Riccardo Casati reports financial support was provided by EIT RawMaterials GmbH. If there are other authors, they declare that they have no known competing financial interests or personal relationships that could have appeared to influence the work reported in this paper.

Acknowledgements

This work was financially supported by PoSAddive – Powder Sheet Additive Manufacturing (EIT RawMaterials, No. 22021).

Data availability

Data will be made available on request.

References

[1] M. Manjaiah, K. Raghavendra, N. Balashanmugam, J. Paulo Davim, Additive Manufacturing, Elsevier, 2021, https://doi.org/10.1016/C2019-0-04429-9.

[2] T. DebRoy, H.L.L. Wei, J.S.S. Zuback, T. Mukherjee, J.W.W. Elmer, J.O. O. Milewski, A.M.M. Beese, A. Wilson-Heid, A. De, W. Zhang, Additive manufacturing of metallic components – process, structure and properties, Prog. Mater. Sci. 92 (2018) 112–224, https://doi.org/10.1016/j.pmatsci.2017.10.001.

[3] T. Debroy, T. Mukherjee, J.O. Milewski, J.W. Elmer, B. Ribic, J.J. Blecher, W. Zhang, Scientific, technological and economic issues in metal printing and their solutions, Nat. Mater. 18 (2019) 1026–1032, https://doi.org/10.1038/s41563-019-0408-2.

[4] H. Zhang, J. Hou, X. Liu, D. Sun, Y. Zhu, M. Hao, K. Zhang, A. Huang, X. Tian, Martensitic steels via laser powder-based additive manufacturing: recent advances in process parameters, microstructure tailoring, and mechanical performance, Mater. Des. 258 (2025), https://doi.org/10.1016/j.matdes.2025.114574.

[5] R. Lupoi, W.M. Abbott, R. Senthamaraikannan, S. McConnell, J. Connolly, S. Yin, R.B. Padamati, Metal additive manufacturing via a novel composite material using powder and polymers formed in sheets, CIRP Ann. 71 (2022) 181–184, https://doi.org/10.1016/j.cirp.2022.03.012.

[6] W. Zhang, A. Sasnauskas, A. Coban, S. Marola, R. Casati, S. Yin, R.P. Babu, R. Lupoi, Powder sheets additive manufacturing: principles and capabilities for multi-material printing, Addit. Manuf. Lett. 8 (2024), https://doi.org/10.1016/j.addlet.2023.100187.

[7] T. Fedina, J. Sundqvist, J. Powell, A.F.H. Kaplan, A comparative study of water and gas atomized low alloy steel powders for additive manufacturing, Addit. Manuf. 36 (2020), https://doi.org/10.1016/j.addma.2020.101675.

[8] M.R. Jandaghi, H. Pouraliakbar, L. Iannucci, V. Fallah, M. Pavese, Comparative assessment of gas and water atomized powders for additive manufacturing of 316 L stainless steel: microstructure, mechanical properties, and corrosion resistance, Mater. Charact. 204 (2023), https://doi.org/10.1016/j.matchar.2023.113204.

[9] W. Zhang, A. Coban, A. Sasnauskas, Z. Cai, B. Gillham, W. Mirihanage, S. Yin, R. P. Babu, R. Lupoi, A novel powder sheet laser additive manufacturing method using irregular morphology feedstock, CIRP J. Manuf. Sci. Technol. 52 (2024) 26–35, https://doi.org/10.1016/j.cirpj.2024.05.007.

[10] W. Zhang, S. Marola, S. McConnell, Z. Cai, J.M. Dugenio, M. Li, W.M. Abbott, A. Coban, A. Sasnauskas, S. Yin, R. Padamati Babu, W. Mirihanage, R. Casati, R. Lupoi, Demonstration and benchmarking of a novel powder sheet additive manufacturing approach with austenitic steel, Mater. Des. 245 (2024), https://doi.org/10.1016/j.matdes.2024.113301.

[11] A. Sasnauskas, A. Coban, W. Zhang, W.M. Abbot, R.P. Babu, M.S. Pham, R. Lupoi, Metal additive manufacturing using powder sheets (MAPS) of HEA CoNiCrFeMn: the effect of the polymer content on microstructure and mechanical properties, CIRP Ann. 73 (2024) 173–176, https://doi.org/10.1016/j.cirp.2024.04.066.

[12] M. Abdelwahed, R. Casati, S. Bengtsson, A. Larsson, M. Riccio, M. Vedani, Effects of powder atomisation on microstructural and mechanical behaviour of L-pbf processed steels, Metals 10 (2020) 1474, https://doi.org/10.3390/met10111474.

[13] U. Siemann, Solvent cast technology – a versatile tool for thin film production. Scattering Methods and the Properties of Polymer Materials, Springer Berlin Heidelberg, Berlin, Heidelberg, 2005, pp. 1–14, https://doi.org/10.1007/b107336.

[14] W. Zhang, W.M. Abbott, A. Sasnauskas, A. Coban, B. Gillham, I. Bitharas, S. Lu, J. Quirke, S. Ruan, K. Perkins, K. Synnatschke, M. Moebius, S. Yin, A. Moore, R. P. Babu, R. Lupoi, Development of a novel powder sheets printing process towards the next generation of additive manufacturing: the role of laser defocusing, Virtual Phys. Prototyp. 19 (2024), https://doi.org/10.1080/17452759.2024.2361856.

[15] R. Wang, F. Li, Z. Wu, Y. Kang, J. Fan, Z. Yu, Z. Yan, S. Du, J. Eckert, Precipitation and transformation of carbides during tempering of 7Cr14 Martensitic stainless steel, Steel Res. Int. 95 (2024), https://doi.org/10.1002/srin.202300248.

[16] S. Munusamy, J. Jerald, Effect of in-situ intrinsic heat treatment in metal additive manufacturing: a comprehensive review, Met. Mater. Int. 29 (2023) 3423–3441, https://doi.org/10.1007/s12540-023-01462-2.

[17] R.N. Penha, L.C.F. Canale, J. Vatavuk, S. Lampman, Tempering of steels. Steel Heat Treating Fundamentals and Processes, ASM International, 2018, pp. 327–351, https://doi.org/10.31399/asm.hb.v04a.a0005815.